Re-Examining the First Climate Models: Climate Sensitivity of a Modern Radiative–Convective Equilibrium Model

Lukas Kluft and Sally Dacie

Max Planck Institute for Meteorology, and International Max Planck Research School on Earth System Modelling, and Universität Hamburg, Faculty of Mathematics, Informatics and Natural Sciences, Department of Earth Sciences, Meteorological Institute, Hamburg, Germany

Stefan A. Buehler

Universität Hamburg, Faculty of Mathematics, Informatics and Natural Sciences, Department of Earth Sciences, Meteorological Institute, Hamburg, Germany

Hauke Schmidt and Bjorn Stevens

Max Planck Institute for Meteorology, Hamburg, Germany

(Manuscript received 12 November 2018, in final form 11 July 2019)

ABSTRACT

We revisit clear-sky one-dimensional radiative–convective equilibrium (1D-RCE) and determine its equilibrium climate sensitivity to a CO_2 doubling (ECS) and associated uncertainty. Our 1D-RCE model, named konrad, uses the Rapid Radiative Transfer Model for GCMs (RRTMG) to calculate radiative fluxes in the same way as in comprehensive climate models. The simulated radiative feedbacks are verified by a line-by-line radiative transfer model, with which we also investigate their spectral distribution. Changing the model configuration of konrad enables a clear separation between the water vapor and the lapse rate feedbacks, as well as the interaction between the two. We find that the radiative feedback and ECS are sensitive to the chosen relative humidity profile, resulting in an ECS range of 2.09–2.40 K. Using larger CO_2 forcings we find that the radiative feedback changes up to 10% for surface temperatures of 291–299 K. Although the ECS is similar to previous studies, it arises from the compensation of a larger clear-sky forcing ($4.7\,\mathrm{W\,m^{-2}}$) and more strongly negative feedbacks ($-2.3\,\mathrm{W\,m^{-2}\,K^{-1}}$). The lapse rate feedback and the feedback from the interaction of lapse rate and humidity compensate each other, but the degree of compensation depends on the relative humidity profile. Additionally, the temperature profile is investigated in a warming climate. The temperature change at the convective top is half as large as at the surface, consistent with the proportionally higher anvil temperature hypothesis, as long as the humidity is consistently coupled to the temperature profile.

1. Introduction

Equilibrium climate sensitivity (ECS), the change in surface temperature in response to a doubling of atmospheric CO_2, is arguably one of the most important quantities when discussing climate change. Since the pioneering work by Manabe and Wetherald (1967), a hierarchy of models has been developed to simulate Earth's reaction to an external forcing. But even for the most simple models in this hierarchy, such as radiative–convective equilibrium (RCE) under fixed relative humidity, the value of the ECS is not known with precision (Schlesinger 1986), which makes constraining ECS for more realistic scenarios a challenge that continues to this day (Stevens et al. 2016).

The simple framework of one-dimensional RCE is fundamental to the understanding of climate change. Such a framework forms the theoretical backdrop against which more complex models have been developed and compared, and has greatly influenced the climate debate since its very beginning (National Research Council 1979).

In this paper we report on efforts to formulate a precise RCE problem, estimate its ECS, and explore its

sensitivity to its numerical formulation and the choice of the assumed relative humidity profile. We assume clear skies, fixed relative humidity, fixed ozone, and a saturated isentropic lapse rate. Not taking clouds into account is a deliberate choice, as their inclusion introduces a considerable number of additional degrees of freedom, which are best tackled separately. The precise formulation of the problem allows other models to be compared to our calculations, thereby establishing a benchmark.

Because it is not immediately clear which relative humidity profile is most representative of the atmosphere's response to warming, or even the extent to which RCE is sensitive to the homogeneity assumption implied by the selection of a single relative humidity profile, we explore the sensitivity of our calculations to different profiles of relative humidity. We do so by constructing an ensemble of different humidity distributions, which allows us to explore how the response to greenhouse forcing depends on the assumed profile.

The clear-sky formulation allows us to address the question as to whether there is a state dependence in the simplest possible representation of the climate system, as has been argued in a number of studies. Meraner et al. (2013), for instance, argue that an enhanced water vapor feedback leads to a state dependence of the ECS, whereas Colman and McAvaney (2009) find a balancing of water vapor and lapse rate feedback in a warmer climate in a global climate model (GCM).

For our RCE simulations we use a radiation scheme that trades accuracy for computational efficiency. By using line-by-line radiative transfer simulations we evaluate the fidelity of these base calculations and pinpoint how different radiative feedbacks are distributed spectrally.

Besides its impact on ECS, water vapor also impacts the temperature profile and its evolution in a warming climate. Hartmann and Larson (2002) described its role as a ''thermostat'' for the temperature of the tops of the deepest clouds in the fixed anvil temperature (FAT) hypothesis. A more general approach that takes changes in static stability into account results in a proportionally higher anvil temperature (PHAT; Zelinka and Hartmann 2010). Both FAT and PHAT are based on the interplay of clear-sky radiation and water vapor. In our study, the RCE model is run with different vertical relative humidity distributions and forced with a wide range of CO_2 concentrations to quantify its agreement with the FAT, or PHAT, hypothesis.

2. Problem formulation

The model is configured in a way to simulate the tropical atmosphere, which is to first order in radiative–convective
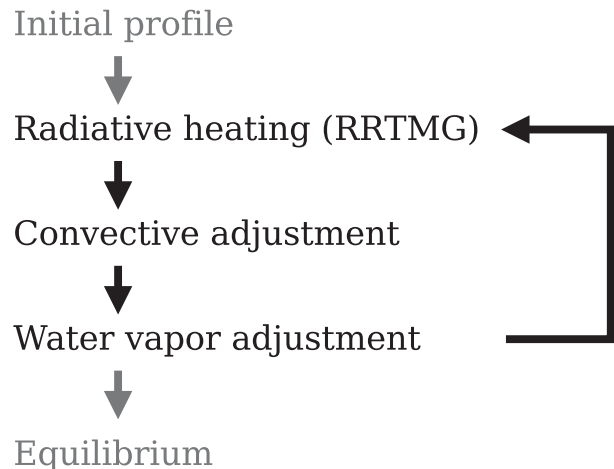
Initial profile

Fig. 1. Illustration of the general model flow. The tasks printed in black are performed iteratively until an equilibrium is found.

equilibrium (Popke et al. 2013). Like the original Manabe and Wetherald (1967) model, the new one-dimensional RCE model (1D-RCE) is based on a radiation scheme that calculates radiative heating for each atmospheric layer (see section 2a). We apply this heating to determine a provisional temperature profile including a coupled surface temperature. Afterward this predicted profile is modified through a convective adjustment (see section 2c). If no convective adjustment is made, the model calculates a pure radiative equilibrium, which results in a convectively unstable thermal structure at lower levels of the atmosphere. Finally, the absolute humidity is recalculated based on the new temperature profile and the assumed relative humidity (see section 2b). Alternatively, the model implements the assumption of fixed absolute humidity, if this step is omitted. The steps are repeated iteratively until an equilibrium state is reached. The full model flow is illustrated in Fig. 1. The model, konrad, is developed under the MIT License and is available on github.com/atmtools/konrad. The simulations in this study have been performed using version 0.6.6 (Kluft and Dacie 2019).

a. Radiation (RRTMG)

For computing radiation, we use the Rapid Radiative Transfer Model for GCMs (RRTMG; Mlawer et al. 1997). RRTMG is used in various GCMs and has been compared to reference radiative transfer models (Pincus et al. 2015). As part of this study, we also compare RRTMG to a benchmark line-by-line code to both test our implementation of RRTMG and assess the sensitivity to the representation of radiative transfer. We use RRTMG through the Climate Modelling and Diagnostics Toolkit (CliMT) Python interface (Monteiro et al. 2018).

Simulations are performed under clear-sky conditions without a diurnal cycle. Thus the choice of the solar geometry attempts to account for these simplifications so as to yield a control simulation that is not too different from conditions representative of the present-day Earth. Just decreasing the solar constant is not sufficient as the optical path through the atmosphere would then be underestimated. Following Cronin (2014) we choose a solar irradiance of 510 W m^{-2} and a zenith angle of 47.88°. This results in an incoming shortwave flux of 342 W m^{-2} at the top of the atmosphere while also keeping the amount of atmospheric absorption in the right proportion. The latter is important for computing radiative heating rates. The configured incoming radiation is lower than observed values in the tropics to compensate for energy transport to the extratropics, which is missing in konrad (Popke et al. 2013). A description of the resultant temperature profile for a present-day atmospheric composition is given in section 3.

RRTMG uses the correlated-k method to allow efficient calculation of fluxes integrated over the full electromagnetic spectrum (Mlawer et al. 1997). The scheme is tuned by using output data from line-by-line models to identify significant parts of the spectrum. The atmospheric states covered by this optimization are based on present-day climate as well as modified conditions like a doubling of CO_2 concentration. Errors (other than those associated with an incorrect implementation) can occur when the climate differs significantly from the underlying reference (e.g., strongly increased CO_2 or temperatures that exceed precalculated lookup tables). We compared the longwave heating rates for different equilibrium states to the line-by-line radiative transfer model ARTS (Atmospheric Radiative Transfer Simulator; Buehler et al. 2018; Eriksson et al. 2011). The differences found are smaller than 0.1 K day^{-1} in the troposphere and smaller than 0.6 K day^{-1} above the tropopause, in agreement with a comparison by Pincus et al. (2015). In addition, a comparison between the radiative feedbacks calculated using RRTMG and ARTS is given in section 4e.

b. Atmospheric state

The atmosphere is discretized in mass space, and thus we adopt fixed pressure p coordinates. The pressure grid is constructed using linearly increasing step sizes in $\ln(p)$ and is approximately given by

$$\ln(p/p_t) = \ln(p_s/p_t)\left(1 - \frac{i^2}{2N^2} - \frac{i}{2N}\right), \qquad (1)$$

with surface pressure p_s (1000 hPa), pressure at model top p_t (1 Pa), and level index i in the range of $[0, N]$. This ensures adequate resolution of the upper stratosphere

TABLE 1. Volume mixing ratios (VMR) of different gases following the RCEMIP configuration (Wing et al. 2018).

Gas	VMR
O_2	21%
CO_2	348 ppmv
CH_4	1650 ppbv
N_2O	306 ppbv
CO	0

while keeping a sufficient number of grid points in the troposphere. The latter is important to resolve changes of the convective top and the cold-point tropopause height more accurately.

We performed simulations with the number of vertical levels ranging from 100 to 1000. The equilibrium surface temperatures for the lowest and highest vertical resolution differ by about 0.3 K. The difference vanishes with increasing number of levels and only affects absolute temperatures; the climate sensitivity is almost independent of the vertical resolution. In the following, simulations are performed with 500 vertical levels to better resolve the tropopause region. Our model atmosphere includes prescribed vertical profiles of relative humidity and ozone as a function of p. In addition, several gases with constant volume mixing ratios are included (see Table 1). The trace gas concentrations are chosen to be consistent with the ones used for the Radiative–Convective Equilibrium Model Intercomparison Project (RCEMIP; Wing et al. 2018).

The ozone volume mixing ratio is a function of pressure p and is also chosen to follow the RCEMIP prescription:

$$O_3(p) = g_1\left(\frac{p}{1 \text{ hPa}}\right)^{g_2}\exp\left(-\frac{p}{g_3}\right), \qquad (2)$$

where $g_1 = 3.6478$ ppmv, $g_2 = 0.832\,09$, and $g_3 = 11.3515$ hPa. The ozone profile is set in the beginning of the simulation and kept constant throughout the whole simulation. In a companion study, we investigate how changes in this profile affect the equilibrium state (Dacie et al. 2019).

As baseline for the troposphere, we prescribe the vertical relative humidity distribution as a function of p in the same way as Manabe and Wetherald [1967, their Eq. (3)]:

$$\text{RH}(p) = \text{RH}_s\frac{p/p_s - 0.02}{1 - 0.02} \qquad (3)$$

with relative humidity at the surface RH_s (77%) and surface pressure p_s (1000 hPa).

This profile differs from the observed mean state of humidity mostly through the lack of a secondary peak in the upper troposphere. Our motivation for choosing this profile was the comparison to the historical study as well as the simplicity of its specification. In sections 4d and 5b, we explore the consequences of this assumption by investigating how our results change for a vertically uniform relative humidity as well as a profile with a second upper-tropospheric humidity peak.

Relative humidity is defined with respect to saturation over water for temperatures above 0°C and with respect to saturation over ice for temperatures below −23°C. For intermediate temperatures the equilibrium pressure is computed as a combination of the values over water and ice according to the Integrated Forecasting System (IFS) documentation [ECMWF 2018, their Eq. (12.13)]. The equilibrium pressures are calculated using empirical formulations by Murphy and Koop (2005).

The absolute humidity in the stratosphere is kept constant at the volume mixing ratio found at the cold-point tropopause. This leads to a moistening the stratosphere if the tropopause warms with surface warming.

c. Convective adjustment

Following Manabe and Wetherald (1967), we perform an energy-conserving convective adjustment in the troposphere, which acts to cool the surface and warm the atmosphere. Our implementation of the convective adjustment differs from that described in Manabe and Wetherald (1967) and Liou (2002), and is described in detail in the appendix. Briefly, we adjust our temperature profile to the saturated isentropic lapse rate, thus taking into account potential energy changes and contribution from the enthalpy of vaporization associated with convection in a saturated column. Although the relative humidity profile is not saturated, use of the saturated isentropic lapse rate is justified by the assumption that atmospheric convection only occurs in saturated regions, which cover a very small fraction of the tropics but set the temperature profile for the whole tropics in accordance with the weak temperature gradient balance (Sobel and Bretherton 2000; Charney 1963).

The way the convective adjustment redistributes energy results in a distinct convective top. Below this convective top the atmosphere is in a state of radiative–convective equilibrium, and above in a state of radiative equilibrium. In a companion study we explore the consequences of relaxing this hard adjustment (Dacie et al. 2019).

The saturated isentropic lapse rate depends on the atmospheric temperature and pressure and is calculated following Bohren and Albrecht [1998, their Eq. (6.111)]:

TABLE 2. Surface properties and physical constants used within konrad.

Variable	Value
Enthalpy of vaporization l_v	2501 k J kg^{-1}
Gravitational acceleration g	9.81 m s^{-2}
Gas constant (dry air) R_d	287.06 J kg^{-1} K^{-1}
Gas constant (water vapor) R_v	461.52 J kg^{-1} K^{-1}
Specific heat capacity c_p	1003.5 J K^{-1}
Surface albedo	0.2
Surface depth	50 m
Surface density	1025 kg m^{-3}
Surface heat capacity	4185.5 J kg^{-1} K^{-1}

$$\frac{dT}{dz} = -\frac{g}{c_p} \frac{1 + l_v w_s / R_d T}{1 + l_v^2 w_s / c_p R_v T^2}, \qquad (4)$$

with gravitational acceleration g, isobaric specific heat capacity c_p, enthalpy of vaporization l_v, saturation mixing ratio w_s, gas constants for the surrounding (dry) air R_d and water vapor R_v, and temperature T (see Table 2 for values). As a simplification l_v is assumed to be constant, thus not varying with temperature.

The assumed lapse rate does not account for fusion enthalpies and thus neglects contributions from the ice phase. The saturated isentropic lapse rate allows a temperature feedback to be taken into account: In a warming climate, the saturated isentropic lapse rate gets less steep, because ascending saturated air parcels are moister and therefore release more latent heat. Hence, the upper troposphere will warm more than the surface (Manabe and Stouffer 1980, their section 5). The strength of this lapse rate feedback is quantified alongside other decomposed feedbacks in section 4c.

d. Surface

We assume a slab surface with an albedo of 0.2 and a heat capacity of 215 MJ m^{-2} K^{-1}. It can be interpreted as being a well-mixed ocean with a depth of 50 m. The heat capacity damps the surface warming rate and prevents strong vertical temperature changes, which could otherwise occur in single time steps. The chosen total heat capacity of the surface is a significant tuning parameter for the time scales of the model. For our studies, however, only the equilibrium states are relevant, which we have verified as being independent of the chosen heat capacity. Chosen surface constants are given in Table 2.

3. Control climate

Figure 2 shows the equilibrium temperature profiles for different CO_2 concentrations as well as a temperature climatology for comparison. The climatology is
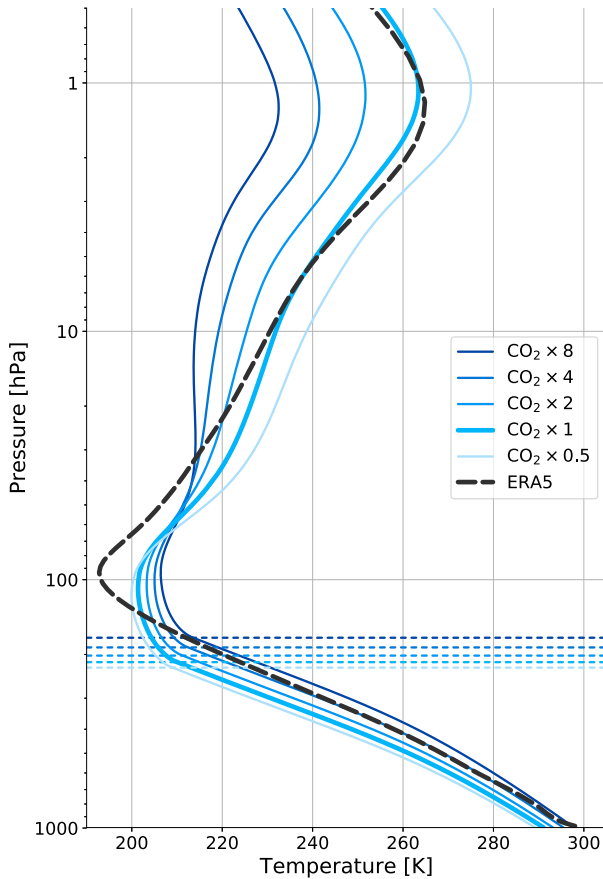
FIG. 2. Equilibrium temperature profiles for different CO_2 concentrations (colors). For each profile the convective top is marked in dashed lines. The ERA5 tropical temperature climatology is shown in dashed black. The figure is clipped at 0.5 hPa to better visualize the troposphere.

based on tropical ocean profiles (30°S–30°N) from ERA5 from January 2008 to May 2018.

Konrad captures the temperature structure of the tropical atmosphere as represented by ERA5. The failure of konrad to form a sharper temperature inversion at the tropopause is indicative of the absence of several processes, like overshooting convection and the Brewer–Dobson circulation, both of which act to cool the atmosphere in those heights through adiabatic cooling (Dacie et al. 2019). In addition, radiative effects of clouds may also play a role.

Overall the RCE framework allows us to simulate a tropical temperature profile that is in qualitative agreement with observations. The resulting temperature profile and surface temperature are used as reference for our sensitivity studies.

4. Radiative feedback

a. Comparison to historical setup

In a first experiment, we reproduce the simulations by Manabe and Wetherald (1967) with our RCE model. Konrad is run under different assumptions about the humidity and lapse rate to quantify their effects, especially on feedbacks. The different model configurations are forced with a doubling of CO_2. An overview of the corresponding ECS estimates for konrad as well as historical studies for comparison is given in Table 3.

The most basic configuration is an RCE with fixed absolute humidity distribution and a constant lapse rate of 6.5 K km^{-1}. This configuration has an ECS of 1.34 K, which is in very close agreement with Manabe and Wetherald (1967).

Next, calculations are performed in which the relative humidity is kept constant following the profile specified in Eq. (3). This introduces a positive water vapor feedback that increases the ECS by 1.31 K (+98%) to a value of 2.65 K. This is slightly larger than Manabe and Wetherald (1967); however, Manabe and Wetherald (1975) mention a decrease in sensitivity after incorporating a superior radiation model, consistent with the interpretation that the larger value that they obtain arises from differences in the treatment of the radiative transfer.

Finally, the constant lapse rate is replaced by a saturated isentropic lapse rate. This introduces a negative lapse rate feedback that reduces the surface warming by 0.56 K (−21%). The estimate for an RCE with combined water vapor–lapse rate feedback is 2.09 K, which is in very good agreement with previous clear-sky estimates.

We conclude that the historical ECS estimates are in good agreement with, but slightly higher than, our modern implementation of a 1D-RCE model. The remaining differences are likely attributed to discrepancies in the exact composition of the atmosphere or details in the radiative transfer calculations.

TABLE 3. Equilibrium climate sensitivity (K) for different RCE models and model configurations. The models are konrad, Manabe and Wetherald (1967, here MW67), Manabe and Wetherald (1975, here MW75), and Hunt and Wells (1979, here H79).

Model configuration	konrad	MW67	MW75	H79
Fixed absolute humidity, constant lapse rate (6.5 K km^{-1})	1.34	1.36	—	—
Fixed relative humidity, constant lapse rate (6.5 K km^{-1})	2.65	2.92	—	2.2
Fixed relative humidity, saturated isentropic lapse rate	2.09	—	1.95	1.81

TABLE 4. Surface temperature change ΔT_s (K) and climate feedback λ (W m^{-2} K^{-1}) for different CO_2 forcings. In addition, the decomposed Planck λ_{PL}, water vapor λ_{WV}, lapse rate λ_{LR}, and combined water vapor–lapse rate $\lambda_{WV \wedge LR}$ feedbacks are given.

CO_2	ΔT_s	λ_{PL}	λ_{WV}	λ_{LR}	$\lambda_{WV \wedge LR}$	λ
×0.5	−1.87	−3.76	1.66	−1.86	1.56	−2.37
×2	2.09	−3.63	1.70	−1.88	1.47	−2.34
×4	4.36	−3.55	1.71	−1.90	1.43	−2.32
×8	6.72	−3.48	1.72	−1.92	1.35	−2.32

b. Climate radiative feedback

We study the sensitivity of konrad to an abrupt change in the CO_2 concentration by a factor of 0.5, 2, 4, or 8. The instantaneous radiative forcing for a doubling of the CO_2 concentration is 2.92 W m^{-2} for the reference case, which incidentally is in perfect agreement with the mean of the CMIP5 models found by Collins et al. (2006). However, for different model configurations used throughout this study we find instantaneous forcings between 2.75–3.15 W m^{-2}, which we mainly attribute to differences in the temperature profiles (Huang et al. 2016).

In contrast, the effective radiative forcing, which includes stratospheric adjustment, is 4.73 W m^{-2}, which is larger than the number of 3.7 W m^{-2} often cited in literature. Possible reasons for this deviation from global mean estimates are the different temperature structure (Huang et al. 2016), an overestimation of the stratospheric cooling due to a missing ozone–temperature feedback (Shepherd and Jonsson 2008), and a missing cloud masking effect.

The surface temperature changes for all simulations are given in Table 4. In addition, the climate feedback parameter

$$\lambda = -\frac{\Delta F_{TOA}}{\Delta T_s} \qquad (5)$$

is given. It quantifies how a surface temperature change ΔT_s feeds back to the radiative imbalance ΔF_{TOA}.

The climate feedback parameter λ is determined using a method introduced by Gregory et al. (2004): we regress the radiative imbalance at the top of the atmosphere against the surface temperature change for every time step. The climate feedback parameter is defined as the fitted slope. We exclude the phase of stratospheric adjustment by only using time steps after the net radiative flux reaches its peak. The Gregory method is justified by the almost perfect linear relationship between the radiative imbalance and surface temperature change (see Fig. 3). A comparison of the regression line with the
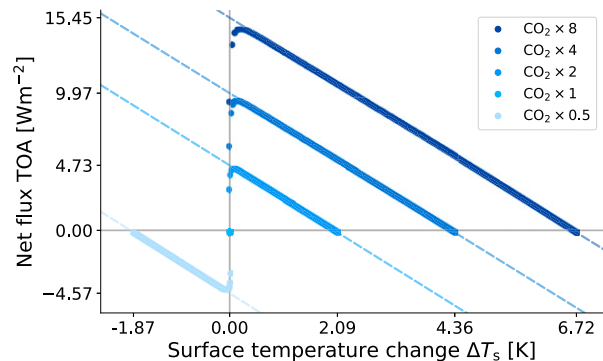

FIG. 3. Top-of-the-atmosphere radiative imbalance against surface temperature change ΔT_s (so-called Gregory plot) for different CO_2 concentrations (colors). A linear regression is shown in dashed lines for each simulation. For different CO_2 concentrations, the x labels highlight ΔT_s and the y labels the effective radiative forcing.

actual data points shows differences that are smaller than 0.05 W m^{-2}.

Figure 3 shows the effective radiative forcing F_{eff} (y intercept of the linear regression), the surface temperature change ΔT_s (x intercept), and climate feedback parameter (slope of the dashed lines) for each simulation. For every doubling in the CO_2 concentration there is an almost constant increase in the simulated surface warming. As a consequence, the total climate feedback parameter is almost constant at 2.33 W m^{-2} K^{-1}. Differences in the temperature change for different CO_2 doublings are mostly attributable to changes in the forcing [a similar increase in forcing with increasing CO_2 is also reported by Gregory et al. (2015)]. Although the radiative transfer becomes increasingly unreliable as one moves away from reference concentrations, konrad runs stably for CO_2 concentrations ranging from 0.25 to 128 times the present-day values and the feedbacks do not diverge substantially from those inferred by extrapolating from the conditions shown here.

c. Decomposed feedbacks

Furthermore, we want to quantify the magnitude of the different radiative feedbacks in konrad. A common approach is the radiative kernel method described by Soden et al. (2008). The method allows response patterns of the Earth system to be transferred into radiative feedbacks using offline radiative transfer simulations. By contrast, our model formulation and the linearity of the climate feedback allow us to decompose the radiative feedback using different model configurations that leave out specific processes:

- The Planck feedback λ_{PL} is defined by the regression of radiative imbalance against surface temperature for

an experiment in which the tropospheric lapse rate and the absolute humidity are fixed constant.

- In the water vapor configuration the relative humidity profile is fixed. The water vapor feedback λ_{WV} is defined as the increase of λ between the Planck and water vapor configuration. Note that, in contrast to existing literature (Soden et al. 2008), this definition of the water vapor feedback does not consider changes in the temperature lapse rate.

- In the lapse rate configuration the temperature profile is convectively adjusted to a saturated isentropic lapse rate that is calculated from the atmospheric state [Eq. (4)] but with fixed absolute humidity. The lapse rate feedback λ_{LR} is defined as the increase of λ between the Planck and lapse rate configuration.

- In the reference configuration the atmosphere is adjusted to a coupled saturated isentropic lapse rate and the relative humidity profile is fixed. Here, the water vapor and lapse rate feedbacks act combined, with introduces a nonlinear feedback caused by the lapse rate–driven increase of upper-tropospheric humidity. We define the magnitude of this additional water vapor–lapse rate feedback $\lambda_{\mathrm{WV}\wedge\mathrm{LR}}$ such that the individual feedbacks add up to the total radiative feedback:

$$\lambda = \lambda_{\mathrm{PL}} + \lambda_{\mathrm{WV}} + \lambda_{\mathrm{LR}} + \lambda_{\mathrm{WV}\wedge\mathrm{LR}}. \qquad (6)$$

In the definition of Soden et al. (2008) the water vapor feedback includes both λ_{WV} and $\lambda_{\mathrm{WV}\wedge\mathrm{LR}}$. The decomposed magnitudes of the Planck, water vapor, lapse rate, and water vapor–lapse rate feedback are shown in Table 4.

The nonconstancy (increase) of the forcing with successive CO_2 doubling is accompanied by a decrease in the strength of the Planck feedback. In addition, there is a slight strengthening of the water vapor feedback due to increased absorption in the atmospheric window (Koll and Cronin 2018). The lapse rate feedback on the order of $1.9\,\mathrm{W\,m^{-2}\,K^{-1}}$ also increases for stronger forcings. When evaluating changes in the feedback parameter one has to keep in mind that different model configurations, including or neglecting different adjustment processes, have different climate sensitivities. As a result, even an eightfold increase in CO_2 does not lead to a large temperature change for the Planck and lapse rate configurations, which are both run with fixed absolute humidity. Considering all adjustment processes in our standard configuration, the changes of the water vapor and the lapse rate feedback have compensating signs, so that their sum is almost constant (Colman and

McAvaney 2009; Cronin and Wing 2017; Soden et al. 2008; Vial et al. 2013).

The additional water vapor–lapse rate feedback is $1.47\,\mathrm{W\,m^{-2}\,K^{-1}}$, close to the value of the water vapor feedback. The combined $\lambda_{\mathrm{WV}\wedge\mathrm{LR}}$ decreases more strongly with the radiative forcing than both λ_{WV} and λ_{LR}. The decrease is on the same order of magnitude as the decrease of the Planck feedback, resulting in an almost constant total feedback (compensating signs). Through our feedback decomposition, we find the upper-tropospheric component of the water vapor feedback ($\lambda_{\mathrm{WV}\wedge\mathrm{LR}}$) to be essential for the compensation. For our simulations, the climate feedback parameter changes by 2.1% across simulations spanning four doublings of the atmospheric CO_2 concentration (Table 4). Over this range the state (temperature) changes by 6.5 K about a working temperature near 295 K. Over the same temperature range, Meraner et al. (2013) estimate a change in sensitivity of 30% (for their constant 80% relative humidity profile), which they attribute to changing feedbacks. Konrad's climate sensitivity changes by 26% for these four doublings, similar to what is reported by Meraner et al. (2013), but almost all of konrad's change can be attributed to the forcing increasing with progressive doublings rather than from changes in feedback. The near constancy of konrad's net feedback arises from a balancing of individual feedbacks, which each change more than their net (see Table 4). Experiments using different solar forcing, much larger changes in CO_2 (both not shown) or different humidity profiles (see section 4d)—which allow us to push the model to much larger temperatures—eventually experience larger changes in sensitivity. This appears to be indicative of larger changes in feedbacks (rather than just forcings) and is being investigated in a further study.

In general, both the radiative forcing and feedbacks are larger than GCM estimates from radiative kernels. The water vapor and lapse rate feedbacks are almost twice as large in magnitude compared to global mean estimates by Soden et al. (2008; for GCMs) and Cronin and Wing (2017; for 3D-RCE). The discrepancy may, to some extent, arise from differences in the spatial sampling. Cronin and Wing (2017) find much larger water vapor feedbacks, in closer agreement with our results, for high surface temperatures in their small-domain 3D-RCE configuration (T. Cronin 2019, personal communication). Another reason may be related to missing cloud masking in our clear-sky configuration. In comprehensive Earth system models the feedback in the middle and lower troposphere might be covered by cloud layers. This interpretation is consistent with the much larger water vapor kernels in the clear as

compared to the all-sky calculations (Soden et al. 2008, their Fig. 2).

d. Sensitivity to assumed water vapor distribution

The assumption of a relative humidity profile that is exponentially decaying with height is not realistic for the tropical atmosphere. Observations have shown that especially the upper troposphere is much more humid (Zelinka and Hartmann 2011) and Minschwaner and Dessler (2004) have found the upper-tropospheric humidity to be important for the climate sensitivity. In the absence of overlying clouds, the midtropospheric humidity also plays an important role in governing the radiative feedback (Soden et al. 2008; Vial et al. 2013). Therefore, we test how our results are affected by the choice of the vertical relative humidity distribution. Although there are more realistic models of the tropical relative humidity distribution (Romps 2014), we deliberately decide to choose models that are simple in their specification.

In the tropical atmosphere, cloud detrainment causes an upper-tropospheric humidity (UTH) peak at the convective top. We modify Eq. (3) by including a UTH peak that is mathematically described using a normal distribution in $\ln(p)$ space:

$$\mathrm{RH_{UTH}}(p) = r_{\mathrm{UTH}} \exp[-\pi \ln^2(p/p_{\mathrm{UTH}})], \qquad (7)$$

with pressure level p_{UTH} and magnitude r_{UTH} (75%) of the peak. The actual relative humidity distribution is given by the maximum of the Manabe model [Eq. (3)] and the UTH peak [Eq. (7)] for each pressure level:

$$\mathrm{RH}(p) = \max\{\mathrm{RH}, \mathrm{RH_{UTH}}\}. \qquad (8)$$

The UTH peak is idealized in order to fulfill two requirements. First, a shift of the UTH peak does not change the relative humidity in the lower troposphere, which also has a significant impact on the climate sensitivity and could obscure possible UTH effects. Second, a shift of the UTH peak does not change its magnitude. Both requirements are necessary to perform comprehensible sensitivity studies. The UTH peak is coupled to the temperature profile by setting its location p_{UTH} equal to the pressure at the convective top as one might expect to happen if convective detrainment levels correlate with the height of the convective top (Zelinka and Hartmann 2010).

Another approach is to assume a vertically uniform relative humidity distribution, which is often used when constructing atmospheric profiles for radiative feedback simulations (Meraner et al. 2013; Koll and Cronin 2018; Thuburn and Craig 2002). We have chosen a vertically
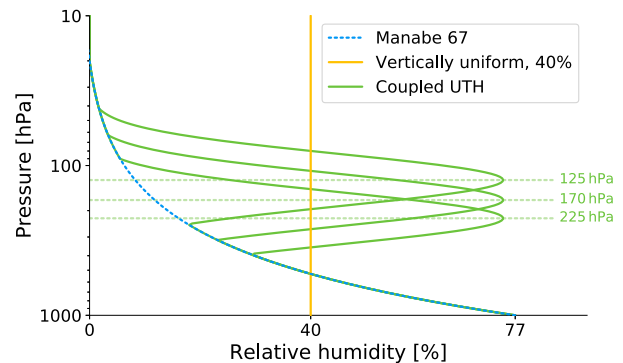

FIG. 4. Idealized vertical distributions of relative humidity: the Manabe and Wetherald (1967) model (blue), a vertically uniform relative humidity of 40% (yellow), and a coupled UTH peak (green; different heights are shown to illustrate how the peak behaves when shifted). The stratospheric water vapor, however, is set constant to the absolute humidity at the cold-point tropopause.

uniform relative humidity of 40% to account for subsaturated subsidence regions, which cover a vast part of the tropics. The chosen distribution also allows us to perform stable simulations over a wide range of radiative forcings. Higher humidities above roughly 60% produce a runaway feedback in konrad. This is in accordance with Pierrehumbert (1995), who finds the tropical atmosphere to be close to a runaway greenhouse if the fraction of subsidence regions, which act as "radiator fins," decreases. In reality, if the tropics alone were close to a runaway greenhouse state and they did warm more than the rest of the planet, transport to middle and high latitudes would also increase.

Figure 4 shows the modified relative humidity profiles with UTH peaks at 125, 170, and 225 hPa (green) alongside the Manabe (blue) and the vertically uniform (yellow) distribution. The relative humidity distribution is used to calculate the water vapor amount in the troposphere. In the stratosphere the absolute humidity is fixed to the volume mixing ratio at the cold-point tropopause.

Experiments were first performed with different surface humidities for each profile (not shown) and indicate that for a given form of the humidity distribution the feedback varies roughly linearly with the integrated water vapor. This approximate linearity justifies the representation of the tropical atmosphere using a mean humidity profile in a single-column model.

Differences in ECS as a function of the given humidity profile are up to 20%. Some of these differences can be explained by the aforementioned, and near-linear, dependence on the integrated water vapor implied by each profile, but the shape of the profile also is important. To explore these effects we decompose the radiative
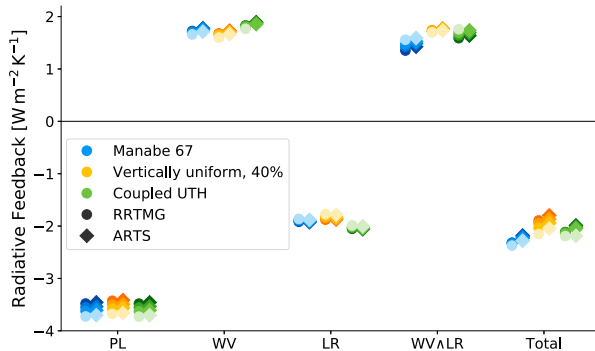
FIG. 5. Decomposed radiative feedbacks for different relative humidity distributions: the reference Manabe and Wetherald (1967) model (blue), a vertically uniform relative humidity of 40% (yellow), and a coupled UTH peak (green). Feedbacks are calculated using the radiation scheme RRTMG (circles), which is used to run the RCE, and an offline line-by-line model ARTS (diamonds) for comparison. Simulations have been performed with forcings of 0.5, 2, 4, and 8 times CO_2 (darker colors indicate higher CO_2 levels).

feedbacks (Fig. 5). The Planck feedback is on the order of $-3.5 \, \mathrm{W \, m^{-2} \, K^{-1}}$ for all humidity distributions. Small differences arise from the fact that the initial states for each relative humidity distribution differ. The weakening of the Planck feedback for stronger forcings (darker colors) due to increased CO_2 absorption is a robust feature for all configurations.

The water vapor feedback is on the order of $1.7 \, \mathrm{W \, m^{-2} \, K^{-1}}$ for all configurations, with the coupled UTH peak giving the strongest feedback of $1.8 \, \mathrm{W \, m^{-2} \, K^{-1}}$. The vertically uniform distribution has a slightly lower feedback compared to the other distributions. This is caused by decreased water vapor absorption in the atmospheric window due to the rather low relative humidity of 40%. All configurations show a slight increase of the water vapor feedback for stronger radiative forcings, which can be explained by a closing of the atmospheric window between 800 and $1200 \, \mathrm{cm^{-1}}$ (Koll and Cronin 2018).

The additional water vapor–lapse rate feedback results from an increase in upper-tropospheric humidity associated with the change in temperature lapse rate. The increase in humidity leads to an upward shift of the emission level to a colder temperature, leading to a positive feedback, which we find to be in the range of 1.47–$1.71 \, \mathrm{W \, m^{-2} \, K^{-1}}$. For the Manabe and coupled UTH distribution, the relative humidity decreases with height, which limits the upward shift of the emission level. As a result, the water vapor–lapse rate feedback decreases under warming. This leads, in combination with an increased Planck feedback, to an almost constant total feedback. For the vertically uniform distribution, however, the

water vapor–lapse rate feedback is almost constant irrespective of the applied warming. As the Planck feedback is no longer balanced, the total radiative feedback λ tends to show a state dependence. The increase of the climate feedback between a doubling and an octupling of the CO_2 concentration is 7.4% for a surface temperature change of about $8 \, \mathrm{K}$.

In summary, the strength of the individual radiative feedbacks depends on the absolute humidity the atmosphere contains and how that humidity is distributed. A vertically uniform humidity distribution prevents a strengthening of the additional water vapor–lapse rate feedback under increased radiative forcing. This leads, in combination with a decreasing Planck feedback, to a slightly larger state dependence of the total climate feedback than for the reference configuration.

e. Comparison to a line-by-line radiative transfer model

We perform line-by-line radiative transfer simulations to verify the radiative feedbacks calculated with RRTMG and to gain insight in their spectral distribution. ARTS is used to calculate the outgoing longwave radiation (OLR) spectrum $E_{\mathrm{OLR}}(\nu)$ on a frequency grid that covers 30 000 equidistant grid points between 1 and $3000 \, \mathrm{cm^{-1}}$. Gas absorption was taken into account by using the HITRAN (high-resolution transmission) database (Gordon et al. 2017) and the MT_CKD model (named for its authors: Mlawer, Tobin, Clough, Kneizys, and Davies) for the continuum absorption of water vapor, CO_2, and molecular nitrogen (Mlawer et al. 2012, version 2.52).

We simulate the OLR after the stratospheric adjustment as well as in equilibrium to calculate the spectral radiative feedback λ_ν, which can be integrated to determine the radiative feedback:

$$\lambda = \int \lambda_\nu \, d\nu = \int \frac{dE_{\mathrm{OLR}}(\nu)}{dT_s} \, d\nu. \qquad (9)$$

Here, the spectral radiative feedback is calculated by dividing the difference of the simulated OLR spectra by the surface temperature change. As ARTS is only capable of simulating the longwave radiative feedback the shortwave component is used from RRTMG. The results are shown as diamonds alongside the RRTMG feedbacks (circles) in Fig. 5. The Planck and lapse rate feedbacks are almost the same for ARTS and RRTMG (differences $\leq 1\%$). We find that RRTMG slightly underestimates the water vapor feedback by about 3% and overestimates the total radiative feedback by about 5%.
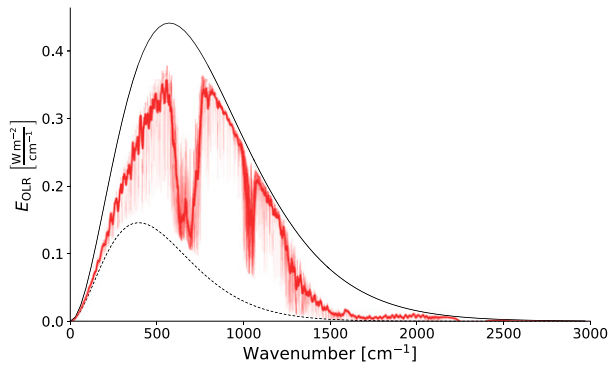
FIG. 6. Outgoing longwave radiation E_{OLR} (thin red line) and the $10\,\text{cm}^{-1}$ running mean (thick red line) as a function of wavenumber. In addition, the blackbody radiation B_ν values at surface temperature (solid black line) and at cold-point temperature (dashed black line) are shown.

The differences seem to be systematic and slightly increase from 4% to 6% for a doubling and an octupling of CO_2 respectively. The comparison to the line-by-line model is robust for all vertical humidity distributions regarded in our study.

In addition, the line-by-line simulations can be used to interpret the spectral fingerprint of different radiative feedbacks. Figure 6 shows the OLR spectrum E_{OLR} for konrad in reference configuration as a qualitative

baseline. In addition, the $10\,\text{cm}^{-1}$ running mean is shown to smooth the fractal character of the spectrum. The spectrum can be qualitatively divided into three spectral regions that are of interest for the radiative feedbacks: first, an atmospheric window region between 800 and $1200\,\text{cm}^{-1}$, in which the overall absorption is weak and limited to water vapor absorption in the lower troposphere; second, the optically thick CO_2 band between 500 and $800\,\text{cm}^{-1}$; and third, a less absorbent region below $500\,\text{cm}^{-1}$ dominated by upper-tropospheric water vapor absorption.

Figure 7 shows the spectral radiative feedbacks for different humidity distributions. The results are smoothed using a $10\,\text{cm}^{-1}$ running mean. In the top-left panel (labeled PL, for Planck), results for konrad in the Planck configuration are shown. The spectral radiative feedback is almost the same for all humidity distributions, with small differences mainly caused by differences in the initial states. As reference, the radiative feedback of a blackbody at surface temperature is shown. The blackbody curve envelops the atmospheric Planck feedback, which is significantly decreased by CO_2 and water vapor absorption.

In the top-right panel, the spectral water vapor (WV) feedback is shown, which is positive throughout the whole spectrum. In the CO_2 band between 500 and
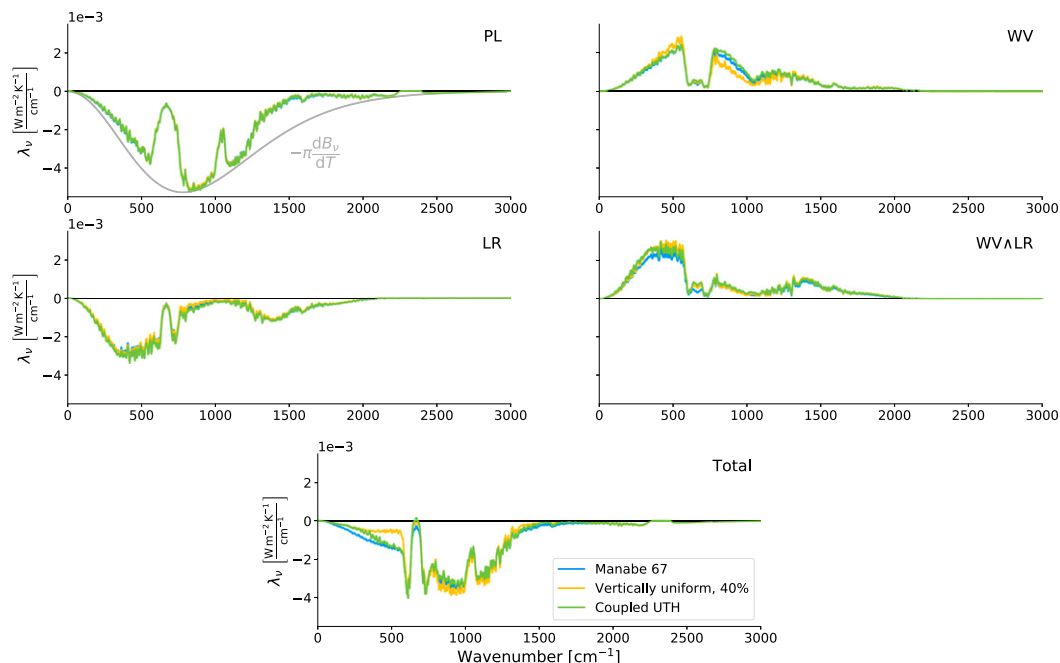

FIG. 7. Decomposed spectral radiative feedback as a function of wavenumber. The Planck (PL), water vapor (WV), lapse rate (LR), combined water vapor–lapse rate (WV∧LR), and total feedbacks have been calculated for different relative humidity distributions. In the panel labeled PL, the temperature derivative of the Planck curve at surface temperature is shown as reference.

$800 \, cm^{-1}$ the water vapor feedback is close to zero (Ingram 2010). Differences in the vertical humidity distribution can be directly observed in the spectral space: The vertically uniform distribution is drier in the lower troposphere than the other distributions, which leads to a smaller radiative feedback in the atmospheric window region between 800 and $1200 \, cm^{-1}$ (Koll and Cronin 2018). In contrast, the radiative feedback below $500 \, cm^{-1}$ is increased due to higher values of upper-tropospheric humidity.

The middle-left panel shows the spectral lapse rate (LR) feedback. The lapse rate feedback is governed by the temperature profile, so the curves are similar for all humidity distributions. The strongest lapse rate feedback is located around $500 \, cm^{-1}$, where the emission level of the OLR is in the upper troposphere, which warms more than the surface. There is another spectral region near $1300 \, cm^{-1}$ where the emission level is similar, but it constitutes much less radiative feedback due to a smaller temperature dependence of the Planck function there.

The additional combined water vapor–lapse rate feedback (WV∧LR) is shown in the middle-right panel. Like the water vapor feedback, it is positive throughout the whole spectrum, but it is mainly dominant for wavenumbers below $500 \, cm^{-1}$, which corresponds to the upper troposphere. The vertically uniform relative humidity results in the strongest water vapor–lapse rate feedback, as a deepening of the troposphere is accompanied by a persistent moistening of the upper troposphere. This leads to the most striking difference in the total spectral radiative feedback, which is the sum of all other feedbacks (bottom panel): For wavenumbers below $500 \, cm^{-1}$ the radiative feedback for the vertically uniform distribution is decreased by a factor of 2 compared to the other humidity distributions.

It is worth noting that the division of the traditional water vapor feedback into two terms, WV and WV∧LR, leads to a deeper understanding of the tendency for intermodel differences between water vapor and lapse rate feedbacks to cancel, as noted by many GCM studies: It is really the intermodel difference in LR and WV∧LR feedbacks that tends to cancel, since both are driven by changes in the tropospheric lapse rate.

Furthermore, it is worth noting that the feedback in the far-infrared spectral region below $600 \, cm^{-1}$ dominates the individual LR, WV, and WV∧LR feedbacks. Due to compensating effects the total feedback is up to an order of magnitude smaller than the individual feedbacks (Ingram 2010; Koll and Cronin 2018). Nonetheless, the total feedback in this region is particularly sensitive to differences in the vertical humidity structure, as it affects the relative strength of the individual feedbacks.

5. PHAT mechanism

a. Historical studies and modern theory

In a next step the vertical temperature structure in and around the tropopause and its evolution under increased CO_2 concentrations are investigated. Early computations of ECS using RCE first started to include clouds on fixed pressure levels (FAP) as this was the easiest approach computationally. It later became apparent that it might be more plausible to consider fixing high clouds at temperature, rather than pressure levels (Augustsson and Ramanathan 1977), an idea whose theoretical justification was formulated in terms of the fixed anvil temperature hypothesis (FAT) by Hartmann and Larson (2002). The chosen approach has a significant impact on ECS, leading to estimates ranging from 1.21 to 2.31 K (Cess 1976; Ramanathan and Coakley 1978). Zelinka and Hartmann (2010) have shown that, if anvil clouds are associated with the maximum radiatively driven divergence, changes in static stability result in proportionally higher anvil temperatures with increasing surface temperature (PHAT). Latest observations and numerical simulations have shown PHAT to be a more realistic description of changes to cloud-top temperatures (Cronin and Wing 2017; Kuang and Hartmann 2007; Zelinka and Hartmann 2010, 2011). As both FAT and PHAT are based on clear-sky radiation, one of them should be verifiable in an RCE framework. We use the temperature at the convective top as proxy for the cloud-top temperature and how it might change with surface warming (Fig. 8).

b. Sensitivity to assumed water vapor distribution

The convective-top temperature in our reference configuration (blue circles) increases 1.17 K for a doubling of the CO_2 concentration, which is roughly half the observed surface temperature change of 2.09 K and a fifth of what FAP predicts. The modified humidity distributions with a coupled UTH have a slightly weaker rate of increase of convective-top temperature with surface warming. Still they are well described by the PHAT hypothesis. Simulations with larger CO_2 perturbations show that this ratio is robust for a wide range of surface temperature changes, consistent with GCM findings by Zelinka and Hartmann (2010).

In a follow-up experiment, the UTH peak is prescribed at different pressure levels between 125 and 225 hPa (every 25 hPa). For these configurations, the present-day equilibrium surface temperatures range from 294.5 to 296.6 K, which is about 1–3 K warmer than the reference. Every model configuration is forced with consecutive CO_2 doublings between 0.5 and 8 times the
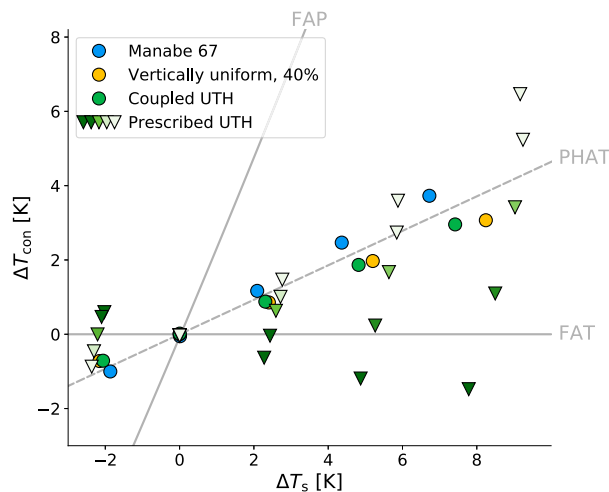
FIG. 8. Change in convective-top temperature ΔT_{con} against change in surface temperature ΔT_s for different CO_2 concentrations and vertical humidity distributions: Manabe and Wetherald (1967) (blue circles), a vertically uniform humidity distribution (yellow circle), UTH peak coupled to the convective top (green circle), and UTH peak at fixed prescribed heights between 125 and 225 hPa [triangles; darker colors represent lower pressure (higher altitude)]. The reference PHAT curve is following Zelinka and Hartmann (2010, their Fig. 9).

present-day concentration. The presence of a fixed UTH peak has a significant impact on the evolution of convective-top temperatures (Fig. 8): Increasing the humidity below the level of the convective top (light green triangles) increases the rate of change of convective-top temperature with surface warming. A UTH peak that is fixed at the initial convective-top pressure is close to the PHAT line, but has a slightly weaker rate of increase of convective-top temperature with surface warming.

Most striking are the results for the two peaks located above the convective top (dark triangles). The additional humidity above the convective top increases the radiative cooling leading to a FAT-like behavior. The highest UTH peak at 125 hPa even leads to negative changes in convective-top temperatures, although this simulation is not realistic, as the UTH peak is rather high, which results in a too-moist lower stratosphere.

We conclude that the PHAT hypothesis describes the change in convective-top temperatures well for the vertical humidity distributions considered in our study. When using a more complex vertical humidity distribution its structure has to be coupled to the temperature profile in order to not artificially distort the PHAT mechanism.

c. Climate sensitivity

The effect of the UTH peaks on ECS can be inferred from the x distance between values in Fig. 8. Coupling

the UTH peak to the convective top results in ECS estimates between the Manabe and a vertically uniform relative humidity distribution. A fixed UTH peak at different prescribed heights results in a spread of ECS estimates from 2.28 to 2.77 K, or feedbacks of −2.24 to −1.79 W m^{-2} K^{-1} respectively. This should be considered when trying to set up "realistic" 1D-RCE simulations using observed relative humidity distributions: imposing a UTH peak that is not properly coupled to the temperature structure will impact the ECS estimate.

6. Summary and conclusions

We defined and performed benchmark calculations for a simple clear-sky RCE problem. The ECS for konrad in reference configuration with fixed relative humidity, fixed ozone, and saturated isentropic lapse rate is 2.09 K, slightly higher than the 1.95 K found by Manabe and Wetherald (1975).

Furthermore, we quantified the decomposed climate radiative feedbacks. The water vapor and lapse rate feedback are almost twice as large in magnitude as global mean estimates, but compensate each other. Possible reasons for their increase are differences in the model region and a missing cloud masking effect in our clear-sky model. We find that a substantial component of the combined water vapor and lapse rate feedbacks comes from the interaction of the two, which explains their degree of compensation in more complex models.

A comparison of different vertical relative humidity distributions results in ECS ranges from 2.09 to 2.40 K with corresponding radiative feedbacks from −2.34 to −2.03 W m^{-2} K^{-1}. Changes in the radiative feedbacks with successive doublings are less than 10% for a range of surface temperatures between 291 and 299 K. The strength of the state dependence itself depends on the shape of the assumed humidity profile: A vertically uniform relative humidity distribution results in an almost constant combined water vapor–lapse rate feedback for different forcings. As the Planck feedback decreases with stronger CO_2 forcings, the total feedback shows tendencies of a state dependency.

The results are robust for a range of CO_2 forcing from 0.5 to 8 times the present-day concentration (i.e., four doublings). A comparison of the radiation scheme RRTMG with the line-by-line model ARTS shows differences in the total climate feedback of about 5%. The errors are of systematic nature and do not substantially increase for stronger forcings.

The change in convective-top temperatures is half as much as the surface temperature change and is consistent with the PHAT hypothesis. The tendency of konrad to verify PHAT rests on the assumption that the relative

humidity profile is coupled to the temperature profile, and departures from PHAT become apparent if they become decoupled.

All results are limited to clear-sky radiation. Future work will explore the implications of extra degrees of freedom as introduced by clouds.

APPENDIX

Instantaneous Adjustment of the Troposphere

A convective adjustment is performed if the atmosphere is unstable to convection in the troposphere. The adjustment fixes the temperatures according to a specified lapse rate, given in kelvins per kilometer, which is converted to kelvins per pascal under the assumption of hydrostatic equilibrium.

The change in enthalpy of an atmospheric layer due to a temperature change $(\Delta T)_{atm}$ is proportional to $\rho c_p (\Delta T)_{atm} dz$, where ρ is the density, c_p is the heat capacity at constant pressure (also assumed to be constant with height), and dz is the thickness of the layer. This can be rewritten (assuming hydrostatic equilibrium) in pressure coordinates as $(c_p/g)(\Delta T)_{atm} dp$, where g is the gravitational acceleration, assumed to be constant with height. The corresponding energy change of the surface is $\Delta z \rho_s c_s (\Delta T)_s$, where Δz is the thickness of the surface layer, ρ_s the density, and c_s the heat capacity. The surface layer is assumed to be at one temperature (it does not vary with depth). Then, the energy conservation equation required for the convective adjustment is

$$\int_0^{p_s} \frac{c_p}{g} (\Delta T)_{atm} \, dp + \Delta z \rho_s c_s (\Delta T)_s = 0. \quad (A1)$$

The integral runs over the whole atmosphere, but there is no convective adjustment above a certain pressure level, p_c, called the convective top. The convective temperature change in the atmosphere $(\Delta T)_{atm}$ is a function of pressure and is given by

$$\Delta T_{atm}(p) = T_{con}(p) - T_{rad}(p), \quad (A2)$$

where T_{rad} is the temperature profile after radiative heating rates have been applied and T_{con} is the convectively adjusted temperature profile:

$$T_{con}(p) = \begin{cases} T_{con,s} - \int_p^{p_s} \gamma_p \, dp & \text{if } p > p_c \\ T_{rad}(p) & \text{if } p \le p_c \end{cases}. \quad (A3)$$

Here, γ_p is the change in temperature of the convective profile with pressure ($\gamma_p > 0$), p_s is the surface pressure, and $T_{con,s}$ is the convectively adjusted surface temperature. We assume that convection acts to cool the surface and warm the troposphere and thus do not allow convection to cool the atmosphere. The pressure level p_c is defined as the highest atmospheric level (lowest pressure level) that satisfies $T_{con}(p_c) \ge T_{rad}(p_c)$ and no convective adjustment is applied above this level.

The equations above, or similar equations with a different treatment of the surface, hold for the convective adjustment of many previous RCE models, including Manabe and Wetherald (1967) and MacKay and Khalil (1991). However, our computational implementation differs. We start with by guessing a surface temperature, $T_{con,s}$ and calculate the corresponding convectively adjusted temperature profile according to Eq. (A3). Then we test how close this profile is to satisfying energy conservation [Eq. (A1)]. We update our surface temperature and repeat the procedure iteratively, until we find a surface temperature and corresponding profile which satisfy Eq. (A1).

REFERENCES

Augustsson, T., and V. Ramanathan, 1977: A radiative–convective model study of the CO$_2$ climate problem. *J. Atmos. Sci.*, **34**, 448–451, https://doi.org/10.1175/1520-0469(1977)034<0448:ARCMSO>2.0.CO;2.

Bohren, C. F., and B. A. Albrecht, 1998: *Atmospheric Thermodynamics.* Oxford University Press, 402 pp.

Buehler, S. A., J. Mendrok, P. Eriksson, A. Perrin, R. Larsson, and O. Lemke, 2018: ARTS, the Atmospheric Radiative Transfer Simulator—Version 2.2, the planetary toolbox edition. *Geosci. Model Dev.*, **11**, 1537–1556, https://doi.org/10.5194/gmd-11-1537-2018.

Cess, R. D., 1976: Climate change: An appraisal of atmospheric feedback mechanisms employing zonal climatology. *J. Atmos.*

Sci., **33**, 1831–1843, https://doi.org/10.1175/1520-0469(1976)033<1831:CCAAOA>2.0.CO;2.

Charney, J. G., 1963: A note on large-scale motions in the tropics. *J. Atmos. Sci.*, **20**, 607–609, https://doi.org/10.1175/1520-0469(1963)020<0607:ANOLSM>2.0.CO;2.

Collins, W. D., and Coauthors, 2006: Radiative forcing by well-mixed greenhouse gases: Estimates from climate models in the Intergovernmental Panel on Climate Change (IPCC) Fourth Assessment Report (AR4). *J. Geophys. Res.*, **111**, D14317, https://doi.org/10.1029/2005JD006713.

Colman, R., and B. McAvaney, 2009: Climate feedbacks under a very broad range of forcing. *Geophys. Res. Lett.*, **36**, L01702, https://doi.org/10.1029/2008GL036268.

Cronin, T. W., 2014: On the choice of average solar zenith angle. *J. Atmos. Sci.*, **71**, 2994–3003, https://doi.org/10.1175/JAS-D-13-0392.1.

——, and A. A. Wing, 2017: Clouds, circulation, and climate sensitivity in a radiative-convective equilibrium channel model. *J. Adv. Model. Earth Syst.*, **9**, 2883–2905, https://doi.org/10.1002/2017MS001111.

Dacie, S., and Coauthors, 2019: A 1D RCE study of factors affecting the tropical tropopause layer and surface climate. *J. Climate*, **32**, 6769–6782, https://doi.org/10.1175/JCLI-D-18-0778.1.

ECMWF, 2018: Part IV: Physical processes. IFS Documentation CY45R1, ECMWF, 223 pp., https://www.ecmwf.int/node/18714.

Eriksson, P., S. A. Buehler, C. P. Davis, C. Emde, and O. Lemke, 2011: ARTS, the Atmospheric Radiative Transfer Simulator, version 2. *J. Quant. Spectrosc. Radiat. Transfer*, **112**, 1551–1558, https://doi.org/10.1016/j.jqsrt.2011.03.001.

Gordon, I. E., and Coauthors, 2017: The HITRAN2016 molecular spectroscopic database. *J. Quant. Spectrosc. Radiat. Transfer*, **203**, 3–69, https://doi.org/10.1016/j.jqsrt.2017.06.038.

Gregory, J. M., and Coauthors, 2004: A new method for diagnosing radiative forcing and climate sensitivity. *Geophys. Res. Lett.*, **31**, L03205, https://doi.org/10.1029/2003GL018747.

——, T. Andrews, and P. Good, 2015: The inconstancy of the transient climate response parameter under increasing CO_2. *Philos. Trans. Roy. Soc.*, **373A**, 20140417, https://doi.org/10.1098/RSTA.2014.0417.

Hartmann, D. L., and K. Larson, 2002: An important constraint on tropical cloud–climate feedback. *Geophys. Res. Lett.*, **29**, 1951, https://doi.org/10.1029/2002GL015835.

Huang, Y., X. Tan, and Y. Xia, 2016: Inhomogeneous radiative forcing of homogeneous greenhouse gases. *J. Geophys. Res. Atmos.*, **121**, 2780–2789, https://doi.org/10.1002/2015JD024569.

Hunt, B. G., and N. C. Wells, 1979: An assessment of the possible future climatic impact of carbon dioxide increases based on a coupled one-dimensional atmospheric-oceanic model. *J. Geophys. Res.*, **84**, 787–791, https://doi.org/10.1029/JC084iC02p00787.

Ingram, W., 2010: A very simple model for the water vapour feedback on climate change. *Quart. J. Roy. Meteor. Soc.*, **136**, 30–40, https://doi.org/10.1002/qj.546.

Kluft, L., and S. Dacie, 2019: atmtools/konrad: A radiative–convective equilibrium model for Python. Zenodo, https://doi.org/10.5281/zenodo.2597967.

Koll, D. D. B., and T. W. Cronin, 2018: Earth's outgoing longwave radiation linear due to H_2O greenhouse effect. *Proc. Natl. Acad. Sci. USA*, **115**, 10 293–10 298, https://doi.org/10.1073/pnas.1809868115.

Kuang, Z., and D. L. Hartmann, 2007: Testing the fixed anvil temperature hypothesis in a cloud-resolving model. *J. Climate*, **20**, 2051–2057, https://doi.org/10.1175/JCLI4124.1.

Liou, K. N., 2002: *An Introduction to Atmospheric Radiation.* 2nd ed. Academic Press, 583 pp.

MacKay, R., and M. Khalil, 1991: Theory and development of a one dimensional time dependent radiative convective climate model. *Chemosphere*, **22**, 383–417, https://doi.org/10.1016/0045-6535(91)90326-9.

Manabe, S., and R. T. Wetherald, 1967: Thermal equilibrium of the atmosphere with a given distribution of relative humidity. *J. Atmos. Sci.*, **24**, 241–259, https://doi.org/10.1175/1520-0469(1967)024<0241:TEOTAW>2.0.CO;2.

——, and ——, 1975: The effects of doubling the CO_2 concentration on the climate of a general circulation model. *J. Atmos. Sci.*, **32**, 3–15, https://doi.org/10.1175/1520-0469(1975)032<0003:TEODTC>2.0.CO;2.

——, and R. J. Stouffer, 1980: Sensitivity of a global climate model to an increase of CO_2 concentration in the atmosphere. *J. Geophys. Res.*, **85**, 5529–5554, https://doi.org/10.1029/JC085IC10P05529

Meraner, K., T. Mauritsen, and A. Voigt, 2013: Robust increase in equilibrium climate sensitivity under global warming. *Geophys. Res. Lett.*, **40**, 5944–5948, https://doi.org/10.1002/2013GL058118.

Minschwaner, K., and A. E. Dessler, 2004: Water vapor feedback in the tropical upper troposphere: Model results and observations. *J. Climate*, **17**, 1272–1282, https://doi.org/10.1175/1520-0442(2004)017<1272:WVFITT>2.0.CO;2.

Mlawer, E. J., V. H. Payne, J.-L. Moncet, J. S. Delamere, M. J. Alvarado, and D. C. Tobin, 2012: Development and recent evaluation of the MT_CKD model of continuum absorption. *Philos. Trans. Roy. Soc.*, **370A**, 2520–2556, https://doi.org/10.1098/rsta.2011.0295.

——, S. J. Taubman, P. D. Brown, M. J. Iacono, and S. A. Clough, 1997: Radiative transfer for inhomogeneous atmospheres: RRTM, a validated correlated-k model for the longwave. *J. Geophys. Res.*, **102**, 16 663–16 682, https://doi.org/10.1029/97JD00237.

Monteiro, J. M., J. McGibbon, and R. Caballero, 2018: sympl (v. 0.4.0) and climt (v. 0.15.3)—Towards a flexible framework for building model hierarchies in Python. *Geosci. Model Dev.*, **11**, 3781–3794, https://doi.org/10.5194/gmd-11-3781-2018.

Murphy, D. M., and T. Koop, 2005: Review of the vapour pressures of ice and supercooled water for atmospheric applications. *Quart. J. Roy. Meteor. Soc.*, **131**, 1539–1565, https://doi.org/10.1256/qj.04.94.

National Research Council, 1979: Carbon dioxide and climate: A scientific assessment. The National Academies Press, 22 pp., https://doi.org/10.17226/12181.

Pierrehumbert, R. T., 1995: Thermostats, radiator fins, and the local runaway greenhouse. *J. Atmos. Sci.*, **52**, 1784–1806, https://doi.org/10.1175/1520-0469(1995)052<1784:TRFATL>2.0.CO;2.

Pincus, R., and Coauthors, 2015: Radiative flux and forcing parameterization error in aerosol-free clear skies. *Geophys. Res. Lett.*, **42**, 5485–5492, https://doi.org/10.1002/2015GL064291.

Popke, D., B. Stevens, and A. Voigt, 2013: Climate and climate change in a radiative–convective equilibrium version of ECHAM6. *J. Adv. Model. Earth Syst.*, **5**, 1–14, https://doi.org/10.1029/2012MS000191.

Ramanathan, V., and J. A. Coakley, 1978: Climate modeling through radiative-convective models. *Rev. Geophys. Space Phys.*, **16**, 465–489, https://doi.org/10.1029/RG016i004p00465.

Romps, D. M., 2014: An analytical model for tropical relative humidity. *J. Climate*, **27**, 7432–7449, https://doi.org/10.1175/JCLI-D-14-00255.1.

Schlesinger, M. E., 1986: Equilibrium and transient climatic warming induced by increased atmospheric CO_2. *Climate Dyn.*, **1**, 35–51, https://doi.org/10.1007/BF01277045.

Shepherd, T. G., and A. I. Jonsson, 2008: On the attribution of stratospheric ozone and temperature changes to changes in ozone-depleting substances and well-mixed greenhouse gases. *Atmos. Chem. Phys.*, **8**, 1435–1444, https://doi.org/10.5194/acp-8-1435-2008.

Sobel, A. H., and Bretherton, C. S., 2000: Modeling tropical precipitation in a single column. *J. Climate*, **13**, 4378–4392, https://doi.org/10.1175/1520-0442(2000)013<4378:MTPIAS>2.0.CO;2.

Soden, B. J., I. M. Held, R. Colman, K. M. Shell, J. T. Kiehl, and C. A. Shields, 2008: Quantifying climate feedbacks using radiative kernels. *J. Climate*, **21**, 3504–3520, https://doi.org/10.1175/2007JCLI2110.1.

Stevens, B., S. C. Sherwood, S. Bony, and M. J. Webb, 2016: Prospects for narrowing bounds on Earth's equilibrium climate sensitivity. *Earth's Future*, **4**, 512–522, https://doi.org/10.1002/2016EF000376.

Thuburn, J., and G. C. Craig, 2002: On the temperature structure of the tropical substratosphere. *J. Geophys. Res.*, **107**, 4017, https://doi.org/10.1029/2001JD000448.

Vial, J., J.-L. Defresne, and S. Bony, 2013: On the interpretation of inter-model spread in CMIP5 climate sensitivity estimates. *Climate Dyn.*, **41**, 3339–3362, https://doi.org/10.1007/s00382-013-1725-9.

Wing, A. A., K. A. Reed, M. Satoh, B. Stevens, S. Bony, and T. Ohno, 2018: Radiative–Convective Equilibrium Model Intercomparison Project. *Geosci. Model Dev.*, **11**, 793–813, https://doi.org/10.5194/gmd-11-793-2018.

Zelinka, M. D., and D. L. Hartmann, 2010: Why is longwave cloud feedback positive? *J. Geophys. Res.*, **115**, D16117, https://doi.org/10.1029/2010JD013817.

——, and ——, 2011: The observed sensitivity of high clouds to mean surface temperature anomalies in the tropics. *J. Geophys. Res.*, **116**, D23103, https://doi.org/10.1029/2011JD016459.